RSC Advances

PAPER

View Article Online
View Journal | View Issue

Cite this: *RSC Adv.*, 2026, **16**, 17905

Interface-engineered N-doped carbon dot/CdSe nanoconjugates as efficient Bi-functional electrocatalysts in alkaline media

Rituparna Dutta,[a] Gokul Sivaguru,[a] Uday Kumar Ghorui,[ab] Aswathi Mangalasseri[a] and Sabyasachi Chakrabortty *[ac]

Electrochemical water oxidation is a cornerstone of sustainable energy technologies, yet its sluggish kinetics demand the design of high-performance, low-cost electrocatalysts. In this study, a rationally designed cost-effective carbon quantum dots/cadmium selenide (CQDs/CdSe) nanocomposite was demonstrated as an efficient electrode material for integrated hydrogen evolution reaction (HER) and oxygen evolution reaction (OER). Furthermore, the hydrothermally synthesized nanocomposite exhibits enhanced charge separation, strong interfacial interactions and a larger number of electroactive sites, leading to improved ion transport and superior conductivity. The CQDs/CdSe nanocomposite revealed low overpotentials of 95 mV and 170 mV for the HER and OER, respectively, at a current density of 10 mA cm^{-2}, with corresponding Tafel slopes of 43 mV dec^{-1} and 63 mV dec^{-1}. The catalyst also demonstrated excellent stability over 50 hours at 50 mA cm^{-2}. A proof-of-concept device with a two-electrode electrolysis set-up was configured using CQDs/CdSe as both the anode and cathode. This device achieved a current density of 10 mA cm^{-2} at 1.77 V, and real-time hydrogen and oxygen evolution was successfully illustrated using a commercial 9-V battery in an H-cell setup. This work highlights the potential of CQD-based hybrid nanostructures as scalable, earth-abundant, intrinsic electrocatalysts for sustainable hydrogen generation.

Received 15th January 2026
Accepted 14th March 2026

DOI: 10.1039/d6ra00371k

rsc.li/rsc-advances

1. Introduction

The rapid industrialization and civilization have led to serious energy concerns, creating the need for clean and sustainable energy development to address the environmental challenges significantly.[1] Addressing this, hydrogen (H_2) fuel has attracted worldwide interest owing to its high gravimetric energy density, renewability, high energy conversion efficiency and zero carbon emissions, with water as a byproduct.[2] Nevertheless, the commercial process of hydrogen production, which includes coal gasification and methane reforming, emits a substantial amount of greenhouse gases.[3] To mitigate the greenhouse gases, water electrolysis (WE) is a key strategy that involves two half-cell reactions, the oxygen evolution reaction (OER) and the hydrogen evolution reaction (HER), occurring simultaneously at the anode and cathode, respectively.[4–7] WE is investigated in both acidic and alkaline media but the acidic system enables faster kinetics in the presence of a high-cost catalyst, while the alkaline system enables slower kinetics in the presence of a low-cost catalyst. In acidic conditions, water splitting benefits from high proton conductivity and a compact cell design but requires expensive noble metal catalysts, such as Pt-group metals (for the HER) and IrO_2 or RuO_2 (for the OER). Despite the faster reaction dynamics in acidic media, poor long-term stability and the corrosive environment limit the practical applicability.[8,9] In contrast, alkaline water splitting could be a promising alternative when low hydrogen cost and large, steady, industrial-scale production are priorities.[10] However, the kinetics of the HER and OER are generally slower due to the involvement of hydroxide ions and dissociation of water molecules, which require additional energy for bond breaking and formation.[11,12] In this context, semiconductor-based catalysts (known as quantum dots (QDs)), such as CdSe, CdS, CdTe, PbS, ZnO, TiO_2, SnO_2, and Fe_2O_3,[13–16] have emerged due to their tunable band structures, electronic characteristics, and surface defects, which enable interfacial charge transfer, modulation of absorption energies, and catalytic selectivity towards the HER and OER processes.[17,18] However, conventional semiconductor systems exhibit inherent drawbacks, such as faster charge recombination, moderate intrinsic conductivity, and insufficient surface-active sites.[19,20] Often, their true potential towards catalytic activity is hindered in pure electrochemical conditions. This

[a]*Department of Chemistry, School of Engineering and Sciences (SEAS), SRM University-AP, Amaravati, Andhra Pradesh 522240, India. E-mail: sabyasachi.c@srmap.edu.in*

[b]*Department of Chemistry, Indian Institute of Technology Gandhinagar, Palaj, Gujarat 382355, India*

[c]*Centre for Interdisciplinary Research, SRM University-AP, Amaravati, Andhra Pradesh 522240, India*

limitation could highlight the need to create a combination of conductive materials to achieve synergism with increased charge transport behaviour and better electrocatalytic activity.

Carbon quantum dots (CQDs), a new class of dimensionally small carbon-based materials, are envisioned as an adoptable nano-modifier, which can improve the electrocatalytic activity, structural stability, tailored defect states, and improved intermediate absorption without being constrained by ineffective charge separation while coupled with QDs.[21,22] CQDs have advantages in strong interfacial connectivity with semiconductors and electrolytes due to the combination of a π-conjugated carbon core with an abundance of available functional groups, *e.g.* –OH, –COOH, and –NH_2, on their surface.[23,24] These attract the CQDs to act as efficient electron mediators, dispersing agents, and defect modulators by electrochemically exposing the active sites, improving the charge transfer kinetics and catalyst stabilization. However, creating true nanoconjugates where CQDs are coupled with QDs *via* chemical bonding or electronic interactions is challenging. On the other hand, their physical mixtures often suffer from inefficient interfacial charge transfer, phase segregation, and poor active site accessibility.[25,26] Thus, the preparation of a nanocomposite based on CQDs-QDs could create proper heterojunctions that can address – (a) molecular level integration, (b) favourable charge separation, and (c) rapid carrier migration across the interface for improved catalytic activities. Such structural and electronic coupling could represent a significant step towards designing active electrocatalysts that exhibit synergism in WE performance.

Additionally, heteroatom doping in carbon nanostructures has been also demonstrated as an efficient method to modulate their local chemical environment and improve charge percolation pathways compared to their pristine counterpart.[27] In general, N, P, S, and B are the most studied atoms that are incorporated into CQDs.[28,29] Especially, N-doping offers well-defined catalytic sites, preserves the conductive sp^2 carbon network, and suitable electronic structures compared to others.[30] Therefore, the combination of N-doped CQDs with CdSe QD as an electrocatalyst could offer a better design strategy, durable and high efficiency material towards the HER and OER.[31–36] Also, similar nanocomposites are well researched in the catalysis domain in terms of their photocatalytic activities.[37,38] However, intrinsic electrocatalytic behaviour, apart from their light-driven effects, would provide us with a better understanding of the true structure–activity relationships in a new nanoconjugate. Thus, we have carefully excluded studies related to complexities in photogenerated carriers, suitable band alignment and optical corrosion. We aim to investigate the fundamental electron transfer dynamics in the nanocomposites before introducing photon-mediated processes, ensuring a comprehensive grasp of their catalytic potential for overall water splitting (OWS).

Considering these advantages of QDs and CQDs, we have introduced a facile hydrothermal synthetic method to engineer a CQDs/CdSe nanocomposite, which was further introduced as an excellent electrocatalyst towards OWS. Their optical characteristics, improved colloidal stability, structures, morphological architectures, and composition analysis were thoroughly studied *via* UV-Vis, TRPL, zeta potential data, XRD, HRTEM and XPS analyses. The synthesized nanocomposite displayed superior interfacial interaction and a higher surface-to-volume ratio, which facilitated a greater number of electroactive sites, leading to an increase in ion transfer kinetics and electrical conductivity within the nanocomposite. Our synthesized CQDs/CdSe nanocomposite displayed a low overpotential of 99 mV and 170 mV for HER and OER processes, respectively, at a current density of 10 mA cm^{-2}. Furthermore, the nanocomposite revealed low Tafel slopes of 43 mV dec^{-1} and 63 mV dec^{-1}, indicating its quicker reaction dynamics for the evolution of H_2 and O_2, respectively, with an extended stability of 50 h at 50 mA cm^{-2}. Additionally, we performed overall water splitting using CQDs/CdSe as the anode and cathode, where the two-electrode setup required 1.77 V to attain 10 mA cm^{-2}. Finally, for real-time applicability, the evolution of H_2 and O_2 was performed in a H-cell setup, which was powered by a commercial 9 V battery.

2. Experimental details

2.1. Chemicals and materials

Ammonium oxalate ($C_2H_8N_2O_4 \cdot H_2O$, SRL, 98% extrapure, 1.40 mmol), urea (CH_4N_2O, SRL, 99% extrapure, 3.4 mmol), anhydrous citric acid ($C_6H_8O_7$, 99% extrapure, SRL), cadmium chloride ($CdCl_2 \cdot H_2O$, SRL, 98% pure, 0.36 mmol), mercaptosuccinic acid ($C_4H_6O_4S$: MSA, 97% pure, Sigma Aldrich, 0.56 mmol), sodium selenite anhydrous (Na_2SeO_3, Loba Chemie, 99% AR), sodium borohydride ($NaBH_4$, SRL), sodium hydroxide pellets (NaOH, Avra, 98%), potassium hydroxide pellets (KOH, 85%, SRL), ethanol (EtOH, Spectrochem Pvt. Ltd), 10% platinum on carbon (10% Pt/C, 99.9% purity, Sigma Aldrich) and ruthenium oxide (RuO_2, 99.9% purity, Sigma Aldrich) were used without any further purification. DI water was used as the solvent for the entire experiment. Ni foam with a thickness of 1.6 mm and dimensions of 2 cm × 1 cm was used as a current collector.

2.2. Synthesis of CQD-modified CdSe composites

The CQDs/CdSe nanocomposites were synthesized *via* a simple, facile and low-cost hydrothermal method. Initially, CQDs were prepared by grinding three different salts, which include ammonium oxalate, urea, and anhydrous citric acid, and the obtained solid was heated at 200 °C for 3 h. Here, urea was used to control the grain size of the particles. Next, the selenium precursor solution was freshly prepared by adding 0.1 g of $NaBH_4$ and 0.2 mmol of Na_2SeO_3 in 5 mL of DI water with constant stirring at room temperature and kept aside for further use. Separately, the synthesized CQDs were added to DI water under vigorous stirring for 2–3 min in a conical flask. Next, 0.36 mmol of $CdCl_2 \cdot H_2O$ and 0.56 mmol of MSA were added to the previous mixture under vigorous stirring, followed by maintaining the pH at ~11 using 1 M NaOH. The MSA acts as a stabilizing agent in the synthesis of nanocomposites. Subsequently, 1 mL of the prepared Se precursors was introduced into the cadmium precursors with constant stirring for 3–5 min.

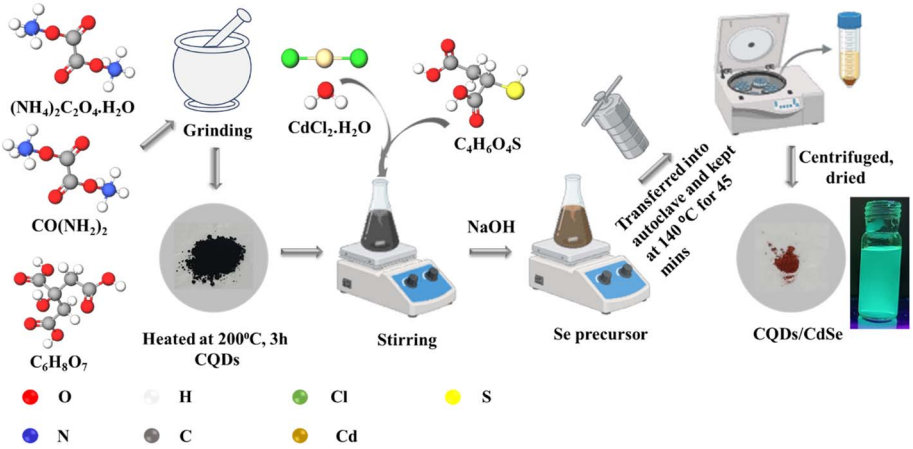

Scheme 1 Synthesis scheme of the prepared CQDs/CdSe NCs.

Subsequently, the solution was transferred into a 100 mL Teflon-lined hydrothermal reactor and placed at a temperature of 140 °C, resulting in the formation of CQDs/CdSe nanocomposites. The autoclave was then cooled to ambient temperature and the resultant product was centrifuged at 4000 rpm with an ethanol–water mixture and finally, washed with ethanol. The precipitate was collected and vacuumed at 60 °C for 12 h and stored for further use. The synthetic procedure is illustrated in Scheme 1.

2.3. Electrode preparation

Nickel foam (NF) was first cut into 2 cm × 1 cm dimensions and cleaned with three distinct solvents. At first, the pieces of NFs were sonicated in 1 M HCl, followed by DI water and finally with ethanol. Then, the cleaned NFs were vacuumed for 12 hours at 60 °C to prevent aerial oxidation. A slurry of PVDF, carbon black, and CQDs/CdSe NCs was prepared in the ratio of 1 : 1 : 8. The prepared slurry was coated onto 1 cm × 1 cm portions of the NFs, which were further vacuum-dried overnight at 60 °C. The active mass loading on the NF was maintained at ~4.5 mg. The same procedure was implemented for the preparation of Pt/C and RuO_2 inks with the same amount of mass loading for better comparison.

2.4. Electrochemical characterization

At room temperature, all the electrochemical measurements were carried out in a three-electrode setup *via* the Admiral Squidstat plus system. The catalyst-coated NFs served as the working electrode, the counter electrode was a platinum spring and the reference electrode used was the silver/silver chloride electrode. The linear sweep voltammetry (LSV) curve of the materials was determined in the range of 1.17 V *vs.* RHE to 2 V *vs.* RHE for the OER and 0.15 V *vs.* RHE to −1 V *vs.* RHE for the HER in 1 M KOH. Electrochemical impedance spectroscopy (EIS) was performed in the range of 100 kHz to 100 mHz. Finally, to investigate the long-term durability of CQDs/CdSe, both the HER and OER were tested for chronoamperometry stability at a potential corresponding to 50 mA cm^{-2} for 50 h. The Ag/AgCl scale was converted to the RHE scale for all the measured potentials using eqn (1).

$$E_{RHE} = E^0_{Ag/AgCl} + 0.197 + 0.059pH \quad (1)$$

where $E^0_{Ag/AgCl}$ corresponds to the measured potential during electrochemical analysis. For the overall water splitting (OWS), we devised a symmetric cell configuration, in which the CQDs/CdSe were used as both the anode and cathode as a bifunctional electrocatalyst.

2.5. Physical characterization

The structural analyses were performed *via* X-ray diffraction (XRD) analysis on an Empyrean Malvern Panalytical Ltd diffractometer within the 2θ range of 10°–90°. The crystal plane spacing, morphology and selected area electron diffraction (SEAD) pattern were visualized using a JEOL (Japan) JEM-2100 Plus high-resolution transmission electron microscope (HRTEM) at a voltage of 200 kV. The chemical states of the materials were identified using X-ray photoelectron spectroscopy (XPS) in PHI VersaProbe III to analyse the sample surface.

3. Results and discussions

3.1. Optical characteristics

The optical characteristics of CQDs, CdSe, and CQDs/CdSe were studied *via* UV-Vis absorption spectra, as depicted in Fig. 1a, where the CQDs exhibited a broad absorption peak at 410 nm, while the CdSe showed a sharp edge excitonic peak at 520 nm. In the CQDs/CdSe nanocomposite, a slight red shift towards 525 nm was observed compared to the pristine materials, indicating a strong interaction between CQDs and CdSe and a possibility of interface formation. This facilitates charge transfer during electrochemical processes by increasing the density of active electrons and holes and enabling effective photocarrier formation.[39] The steady-state photoluminescence (PL) spectra at a 400 nm excitation are shown in Fig. 1b, where the pristine CdSe and CQDs show an emission peak at ~542 nm and ~525 nm, respectively, with a high PL intensity of the latter

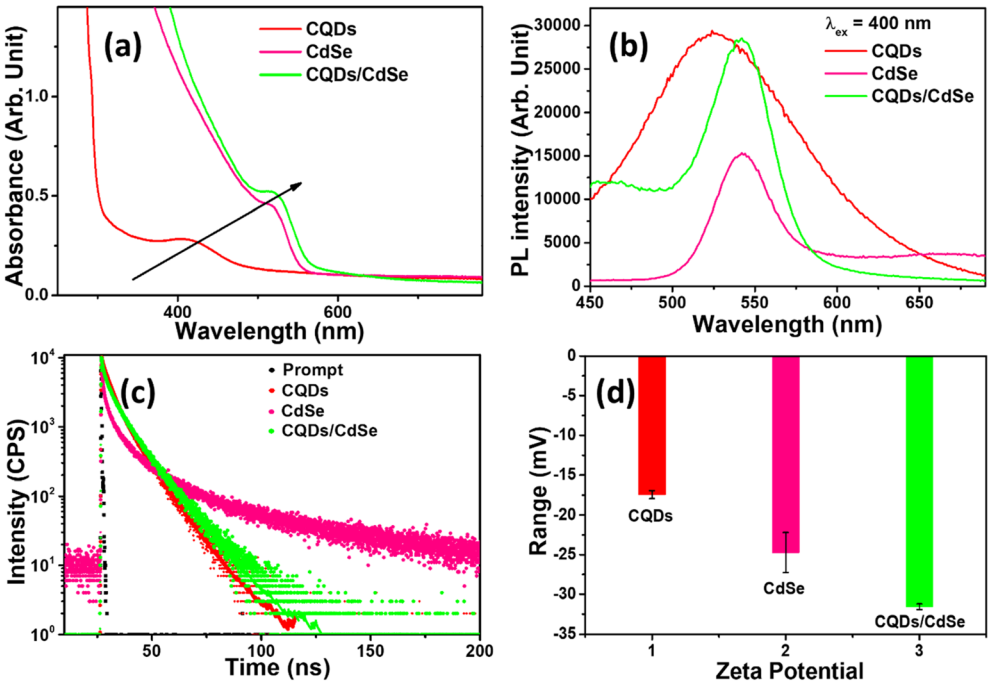

Fig. 1 (a) UV-Vis absorption spectra of CQDs, CdSe, and the CQDs/CdSe nanocomposites showing a red shift (~525 nm), indicating interfacial coupling and extended visible-light absorption. (b) Photoluminescence spectra of the CQD, CdSe, and CQDs/CdSe composite with an excitation wavelength of 400 nm. (c) The recombination dynamics in CQDs/CdSe, compared to pure CdSe and CQDs, are displayed by the TRPL decay profiles. (d) The zeta potential spectra showing the surface charge characteristics and colloidal stability of CdSe, GQDs, and CQDs/CdSe.

with the same optical density between these two. Interestingly, the CQDs/CdSe nanocomposite retained its emission band at the same wavelength as the pristine CdSe, indicating the predominance of the CdSe percentage in the nanocomposite. Additionally, we also observed a noticeable enhancement in the PL intensity of the nanocomposite, which substantiates the integration of CQDs with the CdSe matrix, thereby passivating surface defects and quenching the non-radiative recombination, which in-turn promotes the radiative recombination of photogenerated charge carriers in the nanocomposite.[40,41] The visible shift in the emission is presented in Fig. S1, where the digital images are shown for various samples under UV light excitation. This was further validated by the TRPL spectra, displayed in Fig. 1c, in which the nanocomposite revealed a longer lifetime of 7.9 ns than that of pristine CQDs. This higher lifetime of the nanocomposite originates from the CdSe material. Conversely, the decay of pristine CQDs is dominated by an intermediate radiative channel, a modest ultrafast non-radiative channel, and a considerable long-lived trap contribution, resulting in an average lifetime of 6.7 ns. These dynamics vary significantly in the CQDs/CdSe nanocomposite, where the long trap-related emission is mostly quenched, the ultrafast trap channel is slowed, and the primary component moves to a longer excitonic lifetime ($\tau_2 = 10.90$ ns, $A_2 \approx 62\%$), resulting in a 7.90 ns average lifetime (presented in Table S1). Also, a deep-trap emission present in the CdSe samples, beyond the 600 nm region, was completely cured in the nanocomposite structures, indicating a proper interface formation. Also, the enhancement of PL intensity and longer lifetimes can be explained by the formation of a heterointerface, with (i) passivated surface trap states, (ii) suppressed non-radiative decay pathways, and (iii) promoted intrinsic band-edge radiative recombination in CdSe.[42]

Furthermore, to assess the colloidal stability of the synthesized nanocomposite, the zeta (ζ) potential values were measured and presented in Fig. 1d, and the values are tabulated in Table S2. This observation aligns with the findings of the zeta potential. The negative surface charge on CQDs is originated from the surface exposed carboxylate group of MSA with capping ligands, which collectively ensure the stability through electrostatic repulsion and steric hindrance.[43] Generally, absolute ζ-potential values higher than ± 30 mV correspond to very stable colloidal systems. As illustrated in Table S2, the ζ-potential value of CQDs/CdSe was -31.56 ± 0.35 mV, which was more negative than the pristine CdSe and CQDs, indicating the better stability of the nanocomposites. This improvement is attributed to the synergetic effect of stabilization and the increased surface functional groups obtained by CQDs, which show better prevention of particle aggregation and better electrode stability during electrocatalysis. The particles that resist aggregation can provide a higher active surface area through the formation of uniform films or dispersions, which can improve the current densities for the HER and OER.[44] Next, the physical traits of the synthesized CQDs/CdSe nanocomposite were studied systematically and are presented in Fig. 2.

3.2. Physical characterizations

X-ray diffraction was performed to analyse the structural characteristics of the synthesized nanocomposite, where peaks

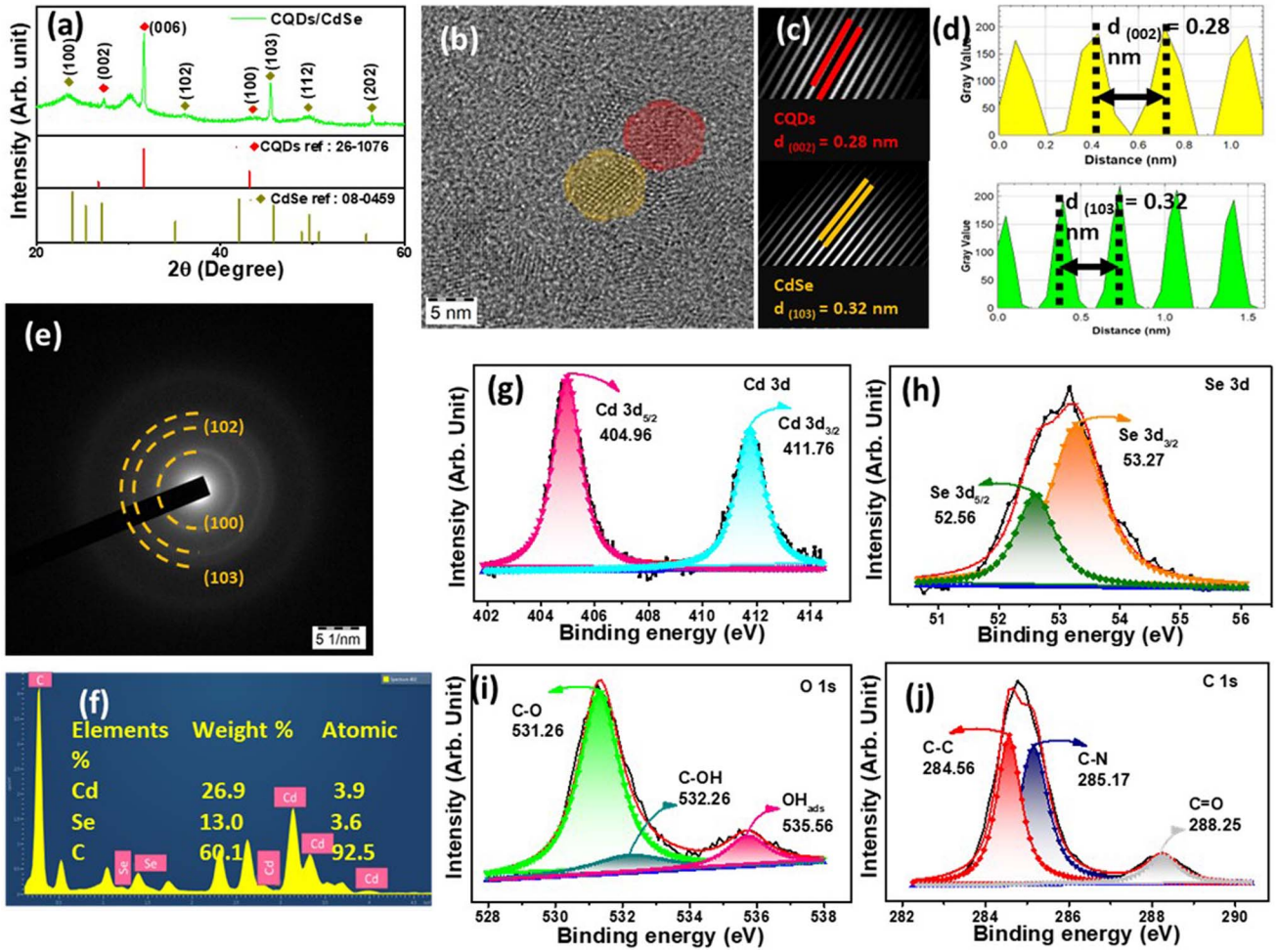

Fig. 2 (a) XRD pattern of the synthesized CQDs/CdSe NCs, which aligns well with the JCPDS reference of CQDs and CdSe. (b) HRTEM image of the synthesized NCs, revealing the interfacial interaction between CQDs and CdSe. (c) Inverse fast Fourier transform of CQDs and CdSe with the respective *d*-spacings. (d) Plot profiles of CQDs and CdSe and the calculation of lattice spacings in CQD/CdSe. (e) SAED pattern of the as-synthesized NCs denoting the *hkl* values of CdSe. (f) EDAX spectra of NCs validating the presence of Cd, Se and C. Deconvoluted XPS spectra of (g) Cd 3d, (h) Se 3d, (i) O 1s and (j) C 1s of CQDs/CdSe.

positioned at 27.23° and 31.68° (in Fig. 2a) correspond to the (002) and (006) planes, respectively, of the CQD matrix (JCPDS: 26-1076). Similarly, the diffraction peaks at 23.43°, 27.23°, 36.07°, 45.48°, 49.54°, and 56.59° correspond to (100), (002), (102), (103), (112), (202) crystal planes, referring to the CdSe QDs (JCPDS: 08-0459). An additional diffraction peak was observed at 30.03°, which might be attributed to the structural or lattice distortion induced by the incorporation of CQDs and contributions from residual phases.[45,46] Interestingly, we observed a shift in peak positions, which might be due to lattice strain induced by interfacial interactions, thereby enhancing the electron transfer rate.[47,48] Also, in the case of pristine CQDs and CdSe (presented in Fig. S2), no significant diffraction peaks were observed, which might arise due to their smaller size. Therefore, the presence of diffraction peaks in the CQDs/CdSe nanocomposite might be due to the formation of a crystalline phase arising from interfacial interactions between CQDs and CdSe. Our synthesis process followed an *in situ* mechanism, in which the promotion of nucleation or growth of CdSe would occur on the heterogeneous nucleation site of CQDs. In that context, the interfacial interaction between CQDs and CdSe reduces the lattice strains and may enhance the ordering by suppressing the amorphous disorder. Furthermore, this validates the co-existence of CQDs and CdSe, which is indicative of the successful formation of the nanocomposite, which was further confirmed from FTIR spectra. Fig. S3 shows the characteristic IR peaks of pristine CQDs, CdSe, and CQDs/CdSe NCs to elucidate their structural changes. CQDs showed five peaks at 3100–3500, 1610, 1370, 1250, and 630 cm^{-1}, which correspond to O–H, combination of C=C and C=O, combination of C–O and COO–, C–N, and C–H stretching vibrations, respectively. The FTIR spectrum of CdSe shows four distinct peaks at 3200–3600, 1590, 1374, and 690 cm^{-1}. The broad band at 3200–3600 cm^{-1} corresponds to O–H, N–H. Next, 1590 cm^{-1} attributed to C=O, C=C, while 1374 cm^{-1} is assigned to C–O, COO^{-}, and 690 cm^{-1} arises from C–H groups. Additionally, IR spectra revealed the presence of all significant stretching vibrations, which suggests the formation of NCs.[49] In addition to this, the

interfacial interaction between CQDs and CdSe and the formation of nanoconjugates were further visualized from the TEM images presented in Fig. 2b. We hypothesize that this interfacial interaction introduces a larger number of catalytically active sites, which enhance the OWS efficiency. Also, the *d* spacing values of CQDs and CdSe in the NCs were found to be 0.28 nm and 0.32 nm, respectively, depicted in Fig. 2c, which aligned well with the (002) plane of CQDs and (103) plane of CdSe. Surprisingly, we observed a slight deviation from the lattice spacing of pristine QDs (Fig. S4). The respective plot profile of the CQDs and CdSe are presented in Fig. 2d. In Fig. 2e, the selected area electron diffraction (SAED) pattern revealed a certain extent of crystallinity in their structures, which aligned well with the respective diffraction patterns. Finally, the EDAX spectrum in Fig. 2f confirms the presence of Cd, Se, and C elements, which was further verified from the survey scan XPS spectra presented in Fig. S5 with the atomic percentage in Table S3.

The resolved spectra of Cd 3d in Fig. 2g exhibit two characteristic peaks at 404.96 eV, 411.76 eV, which correspond to the Cd $3d_{5/2}$ and Cd $3d_{3/2}$ electronic states due to spin–orbit coupling, which was also observed for pristine CdSe, as depicted in Fig. S7b. Next, the Se 3d signal in Fig. 2h was further resolved into two peaks positioned at 52.56 eV and 53.34 eV, which corresponded to Se $3d_{5/2}$ and Se $3d_{3/2}$ electronic states, respectively, and resembled the Se of pristine CdSe presented in Fig. S7c.[50] In the case of O 1s in Fig. 2i, the spectrum was deconvoluted into two sharp peaks due to the presence of MSA on the surface of NCs. The binding energy at 531.26 eV resembled the presence of the C–O state and low intense peaks at 532.26 eV and 535.56 eV defined the C–OH and oxygen/OH* adsorption–chemisorption species from surface water.[43,51] This promotes the adsorption–desorption of OH^- ions at the electrode–electrolyte interface. We assume that the adsorbed oxygen plays a vital role in electrocatalytic energy generation or energy storage application. Finally, the peaks positioned at 284.56, 285.17 eV and 288.25 eV in the C 1s spectrum in Fig. 2j is due to sp^3 and sp^2 carbon moieties, corresponding to C–C, C–N and C=O.[52,53] The N 1s spectrum revealed four distinct signals in Fig. S8c, which are attributed to pyridinic N at 399.62 eV, 399.02 eV, graphitic N or amide C–N at 400.11 eV and oxidized N at 401.11 eV, with peaks appearing closer to those of the pristine CQDs. The incorporation of nitrogen species is evident due to the use of urea, citric acid, and ammonium oxalate as CQDs precursors. Specifically, urea contributed to pyridinic nitrogen functionalities, citric acid confirmed the stabilization of graphitic nitrogen in the carbon framework and ammonium oxalate contributed to oxidized N. The coexisting nitrogen species enhanced the electrical conductivity and active surface area to support the electrocatalytic activity.[54,55] Hence, the diverse nitrogen functionalities within the CQDs framework suggests the presence of functional moieties of CQDs to prevent them from agglomerating to form CQDs/CdSe NCs. Interestingly, we also found a significant shift of Cd 3d, Se 3d, C 1s, and O 1s in the peak signals of CQDs/CdSe NCs from the pristine CQDs and CdSe (presented in Fig. S6–S8), which might be due to the successful formation of a heterojunction between CQDs and CdSe. This heterojunction introduces additional electroactive sites and facilitates optimal adsorption–desorption of reaction intermediates, thereby improving the efficiency of overall water splitting (OWS).

3.3. Electrochemical studies

To elucidate the electrocatalytic activity of the synthesized nanocomposite, LSV curves were determined at a potential sweep of 10 mV s^{-1} in the window of 0.15 V to −1 V *vs.* RHE. The synthesized nanocomposite exhibited a minimal overpotential of 99 mV compared to that of pristine CdSe and comparable η_{10} with the commercial Pt/C (10% Pt loading), benchmark catalyst for the HER at 10 mA cm^{-2}, as depicted in Fig. 3a. Also, it is essential to eliminate solution resistance, which can lead to inaccurate potential measurements. To counter the solution resistance, *iR* compensation was performed using the after-the-scan method by the following equation,

$$E_{\text{corrected}} = E_{\text{measured}} - iR \quad (2)$$

where i is the current response, R is the solution resistance, E_{measured} is the observed potential, and $E_{\text{corrected}}$ is the *iR* corrected potential, and the corresponding *iR* corrected HER displayed in Fig. S10a.[56–58] In the case of CQDs, the chemical leaching of the electrode material was observed (as displayed in Fig. S12), indicating the lack of stability in the CQDs-alone nanostructures, and therefore, we did not perform any control experiment using CQDs. Therefore, all the electrochemical characterisations were performed only for CdSe and CQD/CdSe. To elucidate the HER mechanism of the nanocomposite, in general, there are 3 different kinds of well-proposed mechanisms involved in alkaline media for the evolution of hydrogen, which are (1) $H_2O + e^- + S \rightarrow S - H^*_{ad} + OH^-$ (Volmer), (2) $H_2O + e^- + S - H^*_{ad} \rightarrow H_2 + OH^- + S$ (Heyrovsky) and (3) $2S - H^*_{ad} \rightarrow 2S + H_2$ (Tafel).[59] In context, the smallest Tafel slope suggests the occurrence of a faster Volmer–Heyrovsky pathway, and a relatively larger Tafel slope indicates the slower Volmer–Tafel pathway.[36] The hydrogen evolution pathway was assessed *via* the Tafel slope, presented in Fig. S13 *via* eqn (3),

$$\eta = b \log|j| + a \quad (3)$$

In which b denotes the Tafel slope, η represents the overpotential and j indicates the current density. The synthesized nanocomposite exhibited a minimal Tafel value of 42 mV dec^{-1} compared to the control CdSe (164 mV dec^{-1}) and benchmark catalyst Pt/C (75 mV dec^{-1}), as displayed in Fig. S13a. It is evident from the Tafel slope that the kinetics of H_2 production is more favourable in the CQDs/CdSe nanocomposite than that in CdSe and 10% Pt/C owing to the interfacial and synergistic interactions between CQDs and CdSe, which facilitated the rapid charge transfer. The analysis indicated that the reaction proceeds *via* the Tafel mechanism, with the recombination of adsorbed hydrogen atoms (H + H* → H_2) serving as the rate-determining step, thereby lowering the overpotential and enhancing the electrocatalytic activity.

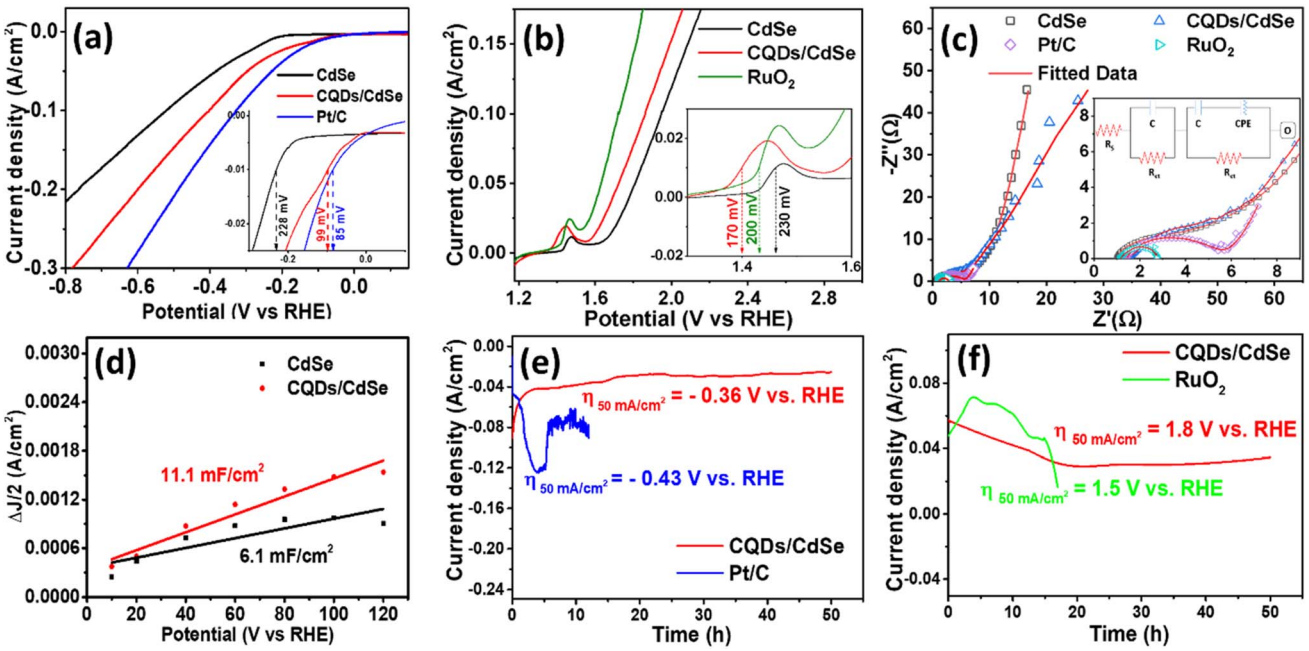

Fig. 3 Linear sweep polarization curves of CdSe, CQDs/CdSe and Pt/C for (a) HER (inset: overpotential at 10 mA cm^{-2}), and (b) OER (inset: overpotential at 10 mA cm^{-2}) performed at 10 mV s^{-1} in 1 M KOH. (c) Electrochemical impedance spectra of CdSe, CQDs/CdSe, Pt/C and RuO_2 from 100 kHz to 100 mHz with the respective circuit diagram provided in the inset, where the CQDs/CdSe displayed a low charge-transfer resistance than the control CdSe, Pt/C and RuO_2. (d) Double-layer capacitance (C_{dl}) of CdSe and CQDs/CdSe for the evaluation of electrochemically active surface area (ECSA). A 50-h chronoamperometric study of CQDs/CdSe compared with the benchmark catalyst Pt/C at 50 mA cm^{-2} for (e) HER, and CQDs/CdSe with RuO_2 at 50 mA cm^{-2} for (f) OER in 1 M KOH.

Similarly, the oxygen evolution ability of the nanocomposite was also studied by implementing LSV polarization in the range of 1.17 V to 2 V. It is clearly evident from Fig. 3b that the CQDs/CdSe nanocomposite displayed a low overpotential of 170 mV compared to that of commercial benchmark catalyst RuO_2 (200 mV) and CdSe (230 mV). However, negative LSV polarization suggests the accurate determination of overpotential at 10 mA cm^{-2} in a similar potential range and the corresponding *iR* corrected OER displayed in Fig. S10b and S11.[60] The characteristic lower overpotential of the nanocomposite might be due to the larger surface area of the zero-dimensional structure that exposes more surface atoms and catalytically active sites, promoting optimum interfacial accumulation and depletion of reactive intermediates.[61] Also, we hypothesize that the successful compositing of CQDs with CdSe improves electrical conductivity by providing an interfacial junction as the catalytically active site, which accelerates the kinetics of O_2 evolution and the charge transfer process at the boundary of the electrode and the electrolyte. This can be further validated by the EIS spectra (Fig. 3c) and minimal Tafel value of 63 mV dec^{-1} in the OER for the CQDs/CdSe nanocomposite, as displayed in Fig. S13b.

The EIS spectra in Fig. 3c display a very low charge-transfer resistance (R_{ct}) for CQDs/CdSe, which validates the effective interaction between CQDs and CdSe, thereby accelerating the charge transfer dynamics and minimizing the overpotential for HER and OER processes.[62] Interestingly, we found a constant phase element (CPE) during the circuit fit of EIS spectra, as displayed in the inset of Fig. 3c. We presume that the presence of CPE relates to porosity, electrochemically active surface area (ECSA) and surface roughness, leading to uneven current distribution, causing the deviation from ideal capacitive behaviour.[63] This can be further confirmed from the ECSA value, which substantiates the low R_{ct} and enhanced electroactivity of the composite. ECSA was evaluated using eqn (4),

$$\mathrm{ECSA} = \frac{C_{dl}}{C_S} \quad (4)$$

where C_{dl} represents the capacitance due to the double layer, calculated from the non-faradaic region of the CV curve presented in Fig. S14 and C_S is the specific capacitance. It is clear from eqn (3) that the ECSA $\propto C_{dl}$, *i.e.*, the ECSA increases with the increase in the C_{dl} value. The ECSA was estimated from double-layer capacitance (C_{dl}), which was measured in the HER region and provided a clear non-faradic window free from overlapping redox transitions presented in the OER region. As the ECSA reflects the intrinsic accessible surface area of the catalyst, the obtained values in the HER region are equally relevant to both HER and OER performances.[64,65] Surprisingly, the nanocomposite displayed a higher C_{dl} value of 11.1 mF cm^{-2} (depicted in Fig. 3d), indicating a higher ECSA value (depicted in Table S4) compared to that of pristine CdSe (6.1 mF cm^{-2}) and closer to the benchmark catalyst (Fig. S15), which corresponds to its higher surface-to-volume ratio with a large number of electroactive sites and quicker reaction dynamics at the electrode electrolyte interface (EEI).[66,67]

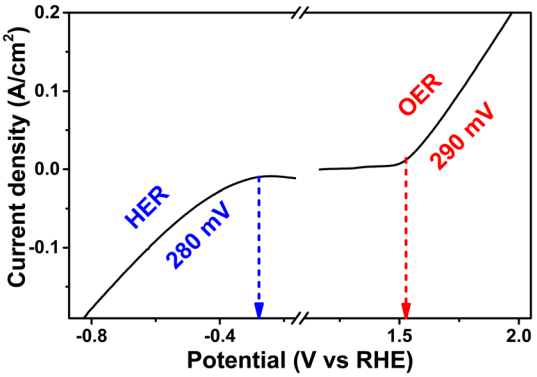

Fig. 4 Linear sweep polarization curve of a physical mixture of CQDs and CdSe for the HER and OER performed at 10 mV s^{-1} in 1 M KOH.

Furthermore, to elucidate the practical applicability of the electrocatalyst, the long-term stability was studied *via* a chronoamperometric technique, where the electrocatalyst was subjected to a potential of −0.36 V *vs.* RHE for the HER (Fig. 3e) and 1.8 V *vs.* RHE for the OER (Fig. 3f), where the current density was achieved at 50 mA cm^{-2}. Interestingly, the catalyst was found to be stable for 50 h, with a slight deviation in current density, which might be due to the initial aggregation of CQDs and surface oxidation occurring at CdSe.[68] As evident from Fig. 3f, the RuO_2 signal exhibits a marked decline, likely originating from the gradual deactivation of active sites during prolonged operation. Additionally, the observed shift could arise from the dissolution of RuO_2 into the electrolyte, potentially forming soluble RuO_2^{2-} species. The findings have been compared with the reported literature and presented in Table S5. In contrast, to justify the strong interfacial interactions between CQDs and CdSe nanocomposites, electrochemical analysis was performed on their physical mixture (Fig. 4).

3.4. Physical mixture of bi-functional NCs

To elucidate the superior electrocatalytic activity of the nanocomposites, electrochemical analysis for a physical mixture of the pristine CQDs and CdSe was attempted. However, it is clearly observed from Fig. S17 that the physical mixture displayed chemical leaching of the electrode, indicating instability and therefore we were not able to conduct the long-time analysis. However, we performed LSV at 10 mV S^{-1} for both the HER and OER side and the corresponding overpotentials were

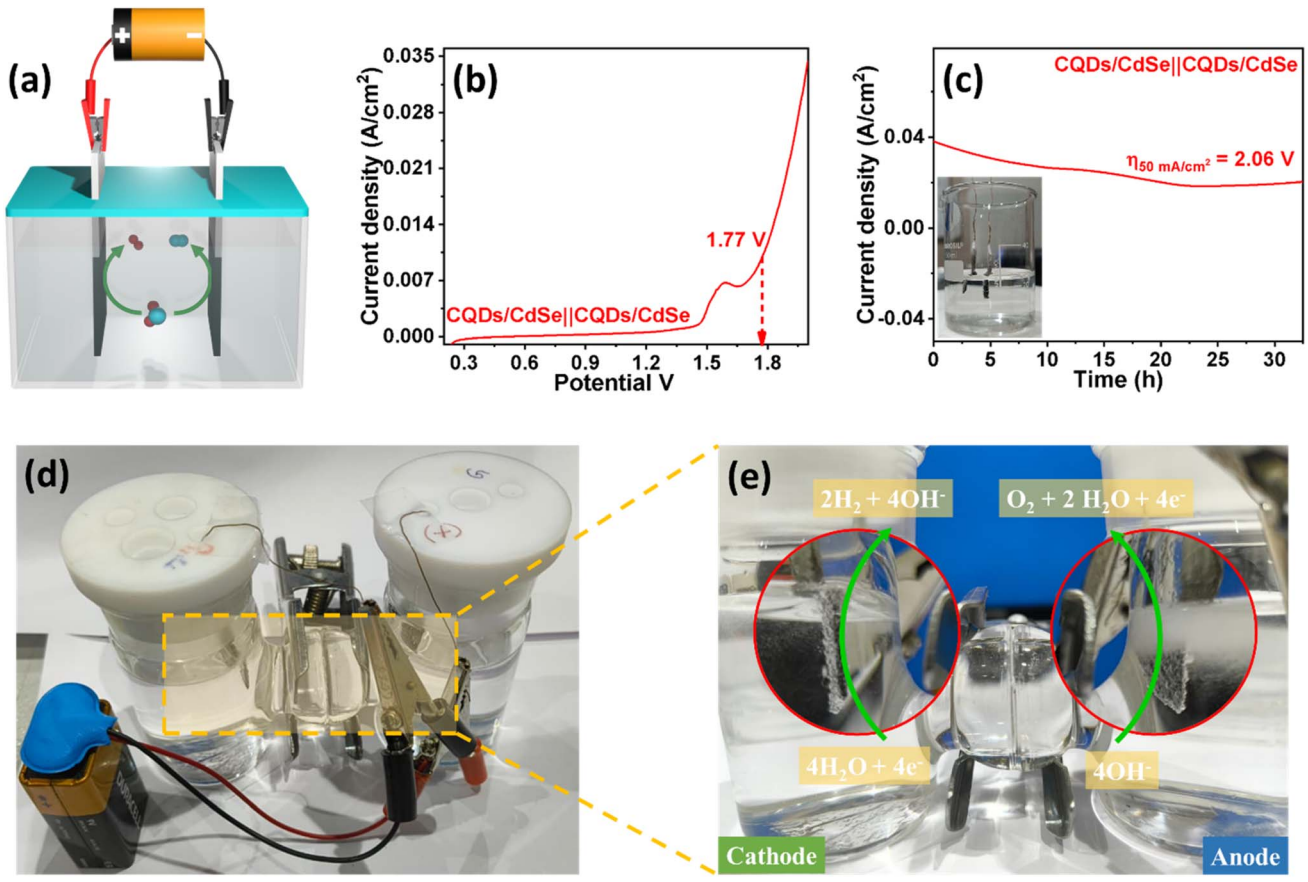

Fig. 5 (a) Schematic of the overall water splitting using CQDs/CdSe as the anode and cathode with a commercial battery. (b) LSV polarization curve of the CQDs/CdSe symmetric cell, where the cell achieved 10 mA cm^{-2} at 1.77 V in 1 M KOH. (c) Chronoamperometric study of the full cell, which was found to be stable up to 32 h at 50 mA cm^{-2}. Inset: performed electrochemical OWS set up. (d) Alkaline water splitting performed with a commercial 9-V battery in 1 M KOH. (e) Enlarged image of the H-cell, where the evolution of hydrogen and oxygen can be seen at the cathode and anode, respectively.

observed as 280 mV and 290 mV for the HER and OER, respectively. Both values were quite high compared to the CQDs/CdSe nanocomposites. Thus, the effectiveness of creating an interface was further established.

3.5. Overall water splitting

Additionally, to scrutinize the real-time applicability as a bi-functional electrocatalyst, we performed overall water splitting (OWS) in a two-electrode system with symmetric construction, where the CQDs/CdSe nanocomposite was used as the anode as well as the cathode, as displayed in Fig. 5a. The LSV curve of the symmetric cell constituting CQDs/CdSe||CQDs/CdSe in 1 M KOH revealed a low overpotential of 1.77 V to attain a current density of 10 mA cm^{-2} (as depicted in Fig. 5b). The *iR* corrected LSV plot is depicted in Fig. S10c. This low overpotential of the CQDs/CdSe symmetric cell might be due to the electronic synchronization interaction between CQDs and CdSe, generating interfacial active sites, which accelerate the HER and OER processes. This was further substantiated by the EIS spectra presented in Fig. S16, where the CQDs/CdSe symmetric cell displayed a low solution as well as charge-transfer resistance. Furthermore, the longevity of the cell was validated using the chronoamperometric technique, where it displayed excellent stability for 32.5 h at 50 mA cm^{-2}, as shown in Fig. 5c. We attributed the initial decrease in current to an activation/equilibration process that involves double-layer stabilization, surface restructuring, and wetting of the electrolyte. After this transient phase, the current stabilizes and reflects in their catalytic activity. To demonstrate the real-world feasibility of the symmetric cell design, we carried out electrolysis using an alkaline electrolyte (1 M KOH solution) in a standard H-cell setup. A Sustainion® membrane was used to ensure the selective transport of hydroxide ions (OH^-) while effectively blocking the migration of unwanted cations. For real-time applicability, the cell was powered by a commercial 9 V battery, as depicted in Fig. 5d. The evolution of H_2 and O_2 at the cathode and anode, respectively, can be clearly visualized in Fig. 5e. Finally, the durability of the electrocatalyst was evaluated through post-catalytic analysis after 33 hours of continuous operation.

3.6. Post-electrocatalysis

After the catalytic cycle, the nature of the electrode material was characterized through XRD and XPS to elucidate the presence of the active species during the electrolysis process, which are further illustrated in Fig. 6a–e. The XRD pattern revealed the preservation of all characteristic peaks of the original electrocatalyst, which confirmed the absence of new crystalline phases during the electrocatalytic process. Notably, we believe that the crystalline nature of the (006) and (103) planes, indexed to a negative shift, would mainly arise after 33 h of electrolysis due to re-constructing.[30] Further, to investigate the changes in the oxidation states of CQDs/CdSe, XPS analysis was performed. Fig. S9 shows the XPS survey spectrum of CQDs/CdSe (after electrocatalysis), which shows the strong signals of Cd 3d, Se 3d, C 1s, and O 1s. Here, the Cd 3d and Se 3d signals originated from CdSe, and C1s and O 1s signals suggest the presence of CQDs in the nanocomposites. Fig. 6b shows the Cd 3d spectra with intense peaks located at 404.94 and 411.74 eV, corresponding to Cd $3d_{5/2}$ and Cd $3d_{3/2}$, respectively. Fig. 6c shows the Se 3d spectra, with peaks indexed at 52.34 and 53.64 eV assigned as Se $3d_{5/2}$ and Se $3d_{3/2}$. However, we did not observe any change in the binding energy of Cd and Se atoms proving their strong electronic coupling.[69] The XPS spectrum of O 1s, as illustrated in Fig. 6d, was deconvoluted into three peaks, in which the peak at 532.44 eV can be attributed to oxygen as a C–

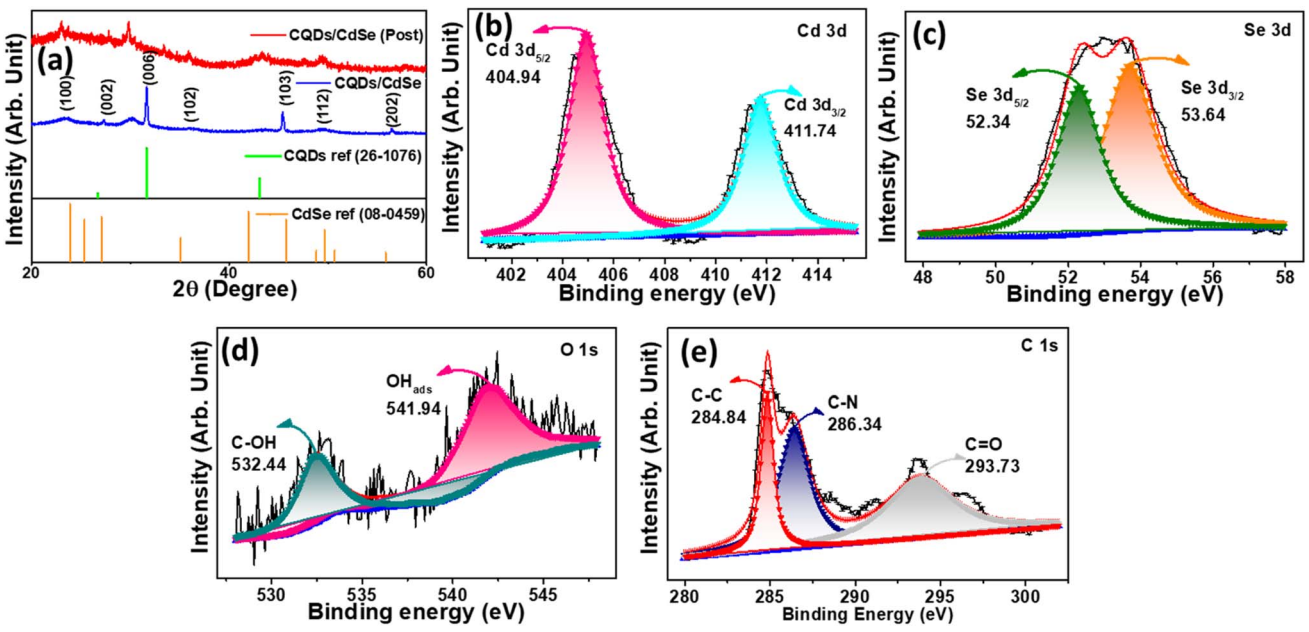

Fig. 6 (a) XRD pattern of the nanocomposite before and after the electrochemical process, Deconvoluted XPS spectra of (b) Cd 3d, (c) Se 3d, (d) O 1s, and (e) C 1s after electrolysis.

OH bond and 541.94 eV correspond to the surface-adsorbed oxygen or adsorbed molecular water.[70] Interestingly, the binding energy shifted from 535.76 eV of the original electrode to 541.94 eV of the post-electrode, which signified that more catalytic active sites and more oxygen vacancies were generated due to the formation of oxide or hydroxide derivatives during electrocatalysis. Similarly, C 1s spectrum is deconvoluted into three signals, corresponding to C–C, C–N, and C=O. In which the C–C and C–N signals show negligible change, however, the persistence of the C=O peak suggests the carbon framework is largely retained and surface restructuring during the catalytic process. Therefore, the prepared bi-functional electrocatalyst is partially transformed into CQDs/CdSe oxides/hydroxides, which further contributes to the excellent electrocatalytic performance towards OWS.

4. Conclusion

In summary, the CQDs/CdSe nanocomposite was successfully synthesized *via* a simple and facile hydrothermal technique with the support of MSA as the capping agent. Due to the existence of interfacial-wall and synergistic interactions (from TEM images) as well as adsorbed oxygen species (from XPS studies), the synthesized nanocomposite displayed superior bi-functional electrochemical activity in both HER and OER processes. Specifically, the synthesized nanocomposite displayed a low solution as well as charge-transfer resistance, owing to its excellent electrical conductivity compared to its pristine counterpart. The electrochemical water splitting of CQDs/CdSe revealed low overpotentials of 99 mV and 170 mV for the HER and OER, respectively, at 10 mA cm^{-2} with excellent stability for 50 h at 50 mA cm^{-2}. Additionally, the CQDs/CdSe-based OWS delivered a current density of 10 mA cm^{-2} at 1.77 V, with prolonged stability for 32.5 h. Finally, we performed alkaline water splitting in an H-cell configuration using a commercial 9 V battery for the production of carbon-free hydrogen fuel. This study presents a simple and cost-effective CQDs/CdSe nanocomposite as a highly efficient electrode material, capable of enabling high-performance energy generation technologies. Their activities are comparable with conventional benchmark catalysts and better than their physical mixtures, establishing a new class of materials consisting of semiconductor-carbon-based electrocatalysts. It can create new avenues for scalable, industrially viable alkaline electrolyzer-based green hydrogen production through the rational design of interfacially-engineered next-generation energy materials.

Author contributions

Conceptualization – RD, UKG, SC; methodology – RD, UKG, SC; validation – RD, UKG, SC; investigation – RD, UKG, SC; resources – RD, UKG, SC; data curation – RD, GS, AM, UKG, SC; writing – original draft – RD, GS, AM, UKG, SC; writing – review & editing – UKG, SC; supervision – SC; project administration – RD, UKG, SC; and funding acquisition – SC. All authors have read and agreed to the published version of the manuscript.

Conflicts of interest

The authors have no competing financial interests to declare.

Data availability

The data that support the findings of the study are available from the corresponding author upon reasonable request.

Supplementary information (SI) is available. See DOI: https://doi.org/10.1039/d6ra00371k.

Acknowledgements

Dr Sabyasachi Chakrabortty acknowledges the financial support from the Anusandhan National Research Foundation (ANRF) under Science & Engineering Research Board (SERB) State University Research Excellence (SERB-SURE) Scheme (SUR/2022/001424), DST-FIST (SR-FST-CS-I-2021-219(C)) and SRM University AP, Andhra Pradesh for an internal research grant (SRMAP/URG/CF/2025-26/087). We acknowledge the Nanotechnology Research Centre (NRC) and SCIF SRM Central Instrumentation Facility, SRMIST, for providing research facilities.

References

1 M. Wang, X. Feng, S. Li, Y. Ma, Y. Peng, S. Yang, Y. Liu, H. Lei, J. Dang, W. Zhang, R. Cao and H. Zheng, Spinel-Type Metal Oxides with Tailored Amorphous/Crystalline Heterointerfaces for Enhanced Electrocatalytic Water Splitting, *Adv. Funct. Mater.*, 2024, **34**(51), 2410439, DOI: 10.1002/adfm.202410439.

2 A. Raveendran, M. Chandran and R. Dhanusuraman, A comprehensive review on the electrochemical parameters and recent material development of electrochemical water splitting electrocatalysts, *RSC Adv.*, 2023, **13**(6), 3843–3876, DOI: 10.1039/d2ra07642j.

3 A. Midilli, H. Kucuk, M. E. Topal, U. Akbulut and I. Dincer, A comprehensive review on hydrogen production from coal gasification: Challenges and Opportunities, *Int. J. Hydrogen Energy*, 2021, **46**(50), 25385–25412, DOI: 10.1016/j.ijhydene.2021.05.088.

4 J. Hao, Z. Zhuang, K. Cao, G. Gao, C. Wang, F. Lai, S. Lu, P. Ma, W. Dong, T. Liu, M. Du and H. Zhu, Unraveling the electronegativity-dominated intermediate adsorption on high-entropy alloy electrocatalysts, *Nat. Commun.*, 2022, **13**(1), 2662, DOI: 10.1038/s41467-022-30379-4.

5 B. Fei, Z. Chen, J. Liu, H. Xu, X. Yan, H. Qing, M. Chen and R. Wu, Ultrathinning Nickel Sulfide with Modulated Electron Density for Efficient Water Splitting, *Adv. Energy Mater.*, 2020, **10**(41), 2001963, DOI: 10.1002/aenm.202001963.

6 Y. Chen and G. Z. Chen, Half-Electrolysis of Water with the Aid of a Supercapacitor Electrode, *ACS Appl. Energy Mater.*, 2023, **6**, 6104–6110.

7 A. Kazemi, F. Manteghi and Z. Tehrani, Metal Electrocatalysts for Hydrogen Production in Water Splitting, *Am. Chem. Soc.*, 2024, **9**(7), 7310–7335, DOI: 10.1021/acsomega.3c07911.

8 Y. Liu, X. Yong, Z. Liu, Z. Chen, Z. Kang and S. Lu, Unified Catalyst for Efficient and Stable Hydrogen Production by Both the Electrolysis of Water and the Hydrolysis of Ammonia Borane, *Adv. Sustain. Syst.*, 2019, **3**(5), 1800161, DOI: 10.1002/adsu.201800161.

9 T. Wang, L. Tao, X. Zhu, C. Chen, W. Chen, S. Du, Y. Zhou, B. Zhou, D. Wang, C. Xie, P. Long, W. Li, Y. Wang, R. Chen, Y. Zou, X. Z. Fu, Y. Li, X. Duan and S. Wang, Combined anodic and cathodic hydrogen production from aldehyde oxidation and hydrogen evolution reaction, *Nat. Catal.*, 2022, **5**(1), 66–73.

10 X. Yu, S. Xu, Z. Wang, X. Cheng, Y. Du, G. Chen, X. Sun and Q. Wu, An Mn-doped NiCoP flower-like structure as a highly efficient electrocatalyst for hydrogen evolution reaction in acidic and alkaline solutions with long duration, *Nanoscale*, 2021, **13**(25), 11069–11076, DOI: 10.1039/D1NR01913A.

11 U. K. Ghorui, G. Sivaguru, U. B. Teja, M. Aswathi, S. Ramakrishna, S. Ghosh, G. K. Dalapati and S. Chakrabortty, Anion-Exchange Membrane Water Electrolyzers for Green Hydrogen Generation: Advancement and Challenges for Industrial Application, *ACS Appl. Energy Mater.*, 2024, **7**(18), 7649–7676, DOI: 10.1021/acsaem.4c01585.

12 J. Zhu, L. Hu, P. Zhao, L. Y. S. Lee and K. Y. Wong, Recent Advances in Electrocatalytic Hydrogen Evolution Using Nanoparticles, *Chem. Rev.*, 2019, **120**(2), 851–918, DOI: 10.1021/acs.chemrev.9b00248.

13 L. Jin, H. Zhao, Z. M. Wang and F. Rosei, Quantum Dots-Based Photoelectrochemical Hydrogen Evolution from Water Splitting, *Adv. Energy Mater.*, 2021, **11**(12), 2003233, DOI: 10.1002/aenm.202003233.

14 W. Li and F. Jäckel, Size-controlled electron transfer rates determine hydrogen generation efficiency in colloidal Pt-decorated CdS quantum dots, *Nanoscale*, 2018, **10**(34), 16153–16158, DOI: 10.1039/C8NR04344B.

15 J.-M. Lee, D.-S. Kim, B. Urupalli, M.-S. Lee, B.-G. Ahn and Y.-T. Yu, Unveiling the potential of alloyed core/double shell InZnP/ZnSe/ZnS quantum dots: High quantum efficiency and stable water splitting performance, *Appl. Catal. O: Open*, 2024, **191**, 206962, DOI: 10.1016/j.apcato.2024.206962.

16 Q. Li, B. Guo, J. Yu, J. Ran, B. Zhang, H. Yan and J. R. Gong, Highly efficient visible-light-driven photocatalytic hydrogen production of CdS-cluster-decorated graphene nanosheets, *J. Am. Chem. Soc.*, 2011, **133**(28), 10878–10884, DOI: 10.1021/ja2025454.

17 S. C. Zhu and F. X. Xiao, Transition Metal Chalcogenides Quantum Dots: Emerging Building Blocks toward Solar-to-Hydrogen Conversion, *ACS Catal.*, 2023, **13**(11), 7269–7309, DOI: 10.1021/acscatal.2c05401.

18 P. Cendula, F. E. Bedoya-Lora and R. R. Prabhakar, Semiconductor Catalysts for Oxygen and Hydrogen Evolution Reactions, *ACS Appl. Energy Mater.*, 2022, **5**(12), 14593–14604, DOI: 10.1021/acsaem.2c02530.

19 A. Mathur, A. Sert and S. Linic, Common Misconceptions in the Analysis of Critical Figures of Merit for Functioning Electrocatalyst/Semiconductor Photoelectrocatalysts under Solar Water-Splitting Conditions, *ACS Energy Lett.*, 2024, **9**(8), 4136–4146, DOI: 10.1021/acsenergylett.4c01365.

20 J. Tan, B. Kang, K. Kim, D. Kang, H. Lee, S. Ma, G. Jang, H. Lee and J. Moon, Hydrogel protection strategy to stabilize water-splitting photoelectrodes, *Nat. Energy*, 2022, **7**(6), 537–547.

21 S. Mandal, S. Adhikari, M. Murmu, B. H. Kim and D. H. Kim, Graphene and Carbon Quantum Dots: Competing Carbons in Harmonized Photoelectrochemical Platforms, *Small*, 2025, **21**(40), e05846, DOI: 10.1002/smll.202505846.

22 S. Dua, P. Kumar, B. Pani, A. Kaur, M. Khanna and G. Bhatt, Stability of carbon quantum dots: a critical review, *RSC Adv.*, 2023, **13**(20), 13845–13861, DOI: 10.1039/d2ra07180k.

23 Z. Liu, W. Hou, H. Guo, Z. Wang, L. Wang and M. Wu, Functional Group Modulation in Carbon Quantum Dots for Accelerating Photocatalytic CO2 Reduction, *ACS Appl. Mater. Interfaces*, 2023, **15**(28), 33868–33877, DOI: 10.1021/acsami.3c05440.

24 M. Fan, Z. Wang, K. Sun, A. Wang, Y. Zhao, Q. Yuan, R. Wang, J. Raj, J. Wu, J. Jiang and L. Wang, N-B-OH Site-Activated Graphene Quantum Dots for Boosting Electrochemical Hydrogen Peroxide Production, *Adv. Mater.*, 2023, **35**(23), 2209086, DOI: 10.1002/adma.202209086.

25 Q. Zhou, X. Yang, X. Xiong, Q. Zhang, B. Peng, Y. Chen, Z. Wang, L. Fu and Y. Wu, A Solid Electrolyte Based on Electrochemical Active Li4Ti5O12 with PVDF for Solid State Lithium Metal Battery, *Adv. Energy Mater.*, 2022, **12**(39), 2201991, DOI: 10.1002/aenm.202201991.

26 E. Payami and R. Teimuri-Mofrad, Ternary nanocomposite of GQDs-polyFc/Fe3O4/PANI: Design, synthesis, and applied for electrochemical energy storage, *Electrochim. Acta*, 2023, **439**, 141706, DOI: 10.1016/j.electacta.2022.141706.

27 B. Jiang, Y. Tian, Y. An, R. Liu and F. Shaik, Electrocatalytic activity analysis of vinegar residue-based heteroatom-doped carbon quantum dots integrated on vertically aligned graphene arrays for hydrogen evolution reaction, *Int. J. Hydrogen Energy*, 2023, **48**, 38686–38698, DOI: 10.1016/j.ijhydene.2023.06.092.

28 N. S. Hafez, E. Z. M. Ebeid, A. Khalifa, S. A. Azim, A. El-Shaer, M. A. S. Sakr and M. B. Z. Hegazy, Modulating carbon quantum dots using multi-heteroatom doping as a bifunctional electrocatalyst for efficient oxygen and hydrogen evolution reactions in alkaline electrolytes, *J. Mater. Chem. A*, 2025, **13**(29), 23454–23462, DOI: 10.1039/D5TA03457D.

29 H. J. Yashwanth, S. R. Rondiya, H. I. Eya, N. Z. Dzade, D. M. Phase, S. D. Dhole and K. Hareesh, Synergy between nitrogen, phosphorus co-doped carbon quantum dots and ZnO nanorods for enhanced hydrogen production, *J. Alloys Compd.*, 2023, **937**, 168397, DOI: 10.1016/j.jallcom.2022.168397.

30 C. Pitchai, S. M. Gopalakrishnan and C. M. Chen, Ultra-efficient Nitrogen-Doped Carbon Dots-Supported Nickel Sulfide as a Platinum-Free Electrocatalyst for Overall Water

Splitting in Basic Medium, *Energy Fuels*, 2024, **38**(3), 2235–2247, DOI: 10.1021/acs.energyfuels.3c03743.

31 J. Cirone, S. R. Ahmed, P. C. Wood and A. Chen, Green Synthesis and Electrochemical Study of Cobalt/Graphene Quantum Dots for Efficient Water Splitting, *J. Phys. Chem. C*, 2019, **123**(14), 9183–9191, DOI: 10.1021/acs.jpcc.9b00951.

32 K. Chandra Majhi, P. Karfa and R. Madhuri, Bimetallic transition metal chalcogenide nanowire array: An effective catalyst for overall water splitting, *Electrochim. Acta*, 2019, **318**, 901–912, DOI: 10.1016/j.electacta.2019.06.106.

33 K. Hareesh, A review on carbon quantum dot/semiconductor-based nanocomposites as hydrogen production photocatalysts, *RSC Adv.*, 2024, **14**(32), 23404–23422, DOI: 10.1039/d4ra04149f.

34 B. S. Reghunath, S. Rajasekaran, S. Devi K R, D. Pinheiro and J. R. Jaleel UC, N-doped graphene quantum dots incorporated cobalt ferrite/graphitic carbon nitride ternary composite for electrochemical overall water splitting, *Int. J. Hydrogen Energy*, 2023, **48**, 2906–2919, DOI: 10.1016/j.ijhydene.2022.10.169.

35 J. Xiao, X. Hou, L. Zhao and Y. Li, A carbon-quantum-dot-sensitized ZnO:Ga/ZnO multijunction composite photoanode for photoelectrochemical water splitting under visible light irradiation, *J. Catal.*, 2017, **346**, 70–77, DOI: 10.1016/j.jcat.2016.11.028.

36 Y. Yan, D. Zhai, Y. Liu, J. Gong, J. Chen, P. Zan, Z. Zeng, S. Li, W. Huang and P. Chen, van der Waals Heterojunction between a Bottom-Up Grown Doped Graphene Quantum Dot and Graphene for Photoelectrochemical Water Splitting, *ACS Nano*, 2020, **14**(1), 1185–1195, DOI: 10.1021/acsnano.9b09554.

37 Y. Yan, J. Chen, N. Li, J. Tian, K. Li, J. Jiang, J. Liu, Q. Tian and P. Chen, Systematic Bandgap Engineering of Graphene Quantum Dots and Applications for Photocatalytic Water Splitting and CO2 Reduction, *ACS Nano*, 2018, **12**(4), 3523–3532, DOI: 10.1021/acsnano.8b00498.

38 F. Khodabandeh, H. Abdizadeh and M. R. Golobostanfard, Decoration of ZnO Nanorod Arrays with Heterojunction of Graphene Quantum Dots and MoS2 Nanoparticles for Photoelectrochemical Water Splitting, *ACS Appl. Energy Mater.*, 2025, **8**, 170–180, DOI: 10.1021/acsaem.4c02240.

39 X. Zou, S. He, G. Teng and C. Zhao, Performance study of CdS/Co-doped-CdSe quantum dot sensitized solar cells, *J. Nanomater.*, 2014, **1**, 818160, DOI: 10.1155/2014/818160.

40 Y. Zhong, W. Chen, S. Yu, Z. Xie, S. Wei and Y. Zhou, CdSe Quantum Dots/g-C3N4 Heterostructure for Efficient H2 Production under Visible Light Irradiation, *ACS Omega*, 2018, **3**(12), 17762–17769, DOI: 10.1021/acsomega.8b02585#_i17.

41 P. D. Wadhavane, R. E. Galian, M. A. Izquierdo, J. Aguilera-Sigalat, F. Galindo, L. Schmidt, M. I. Burguete, J. Pérez-Prieto and S. V. Luis, Photoluminescence enhancement of CdSe quantum dots: A case of organogel-nanoparticle symbiosis, *J. Am. Chem. Soc.*, 2012, **134**(50), 20554–20563, DOI: 10.1021/ja310508r.

42 L. Paul, E. M. Thomas, A. Chemmangat, S. K. Gray and K. G. Thomas, Resonance plasmonic coupling: selective enhancement of band edge emission over trap state emission of CdSe quantum dots, *Chem. Sci.*, 2024, **15**, 20263–20273, DOI: 10.1039/D4SC04960H.

43 S. Bandaru, M. Palanivel, M. Ravipati, W. Y. Wu, S. Zahid, S. S. Halkarni, G. K. Dalapati, K. K. Ghosh, B. Gulyás, P. Padmanabhan and S. Chakrabortty, Highly Monodisperse, Size Tunable Glucosamine Conjugated CdSe Quantum Dots for Enhanced Cellular Uptake and Bioimaging, *ACS Omega*, 2024, **9**(7), 7452–7462, DOI: 10.1021/acsomega.3c04962.

44 F. Davodi, E. Mühlhausen, M. Tavakkoli, J. Sainio, H. Jiang, B. Gökce, G. Marzun and T. Kallio, Catalyst Support Effect on the Activity and Durability of Magnetic Nanoparticles: Toward Design of Advanced Electrocatalyst for Full Water Splitting, *ACS Appl. Mater. Interfaces*, 2018, **10**(37), 31300–31311, DOI: 10.1021/acsami.8b08830.

45 L. Wang, X. Qian, Y. Ren, H. Lei, X. Hu, D. Chen, J. Li and X. Peng, Tuning the Crystal Structure of the Epitaxial CdS Shells on Zinc-Blende CdSe Nanocrystals: Lattice Defects and Electronic Traps, *Chem. Mater.*, 2022, **34**(18), 8297–8305, DOI: 10.1021/acs.chemmater.2c01835.

46 J. Yu, H. V. Demir and M. Sharma, Optical signatures of lattice strain in chemically doped colloidal quantum wells, *Nat. Commun.*, 2025, **16**(1), 823, DOI: 10.1038/s41467-025-55984-x.

47 G. Sivaguru, U. K. Ghorui, M. Girirajan, G. K. Dalapati, P. S. Maram, S. Ghosh, S. Sangaraju and S. Chakrabortty, Rational Design of Asymmetric Spinel/Defect Spinel (ZnMn2O4/Cu1.5Mn1.5O4) Nanocomposite-Based Supercapacitor Devices for Efficient Energy Storage with Improved Cycle Stability, *ACS Appl. Energy Mater.*, 2024, **7**(17), 7205–7219, DOI: 10.1021/acsaem.4c01087.

48 U. K. Ghorui, M. R. A. Sampath, G. Sivaguru, R. Dutta, S. Sangaraju and S. Chakrabortty, B-doped GQD supported cobalt sulfide nanocomposite: A defect engineering approach for superior oxygen electrode performance, *Catal. Today*, 2025, **454**, 115287, DOI: 10.1016/j.cattod.2025.115287.

49 G. S. Bang, G. W. Shim, G. H. Shin, D. Y. Jung, H. Park, W. G. Hong, J. Choi, J. Lee and S. Y. Choi, Pyridinic-N-Doped Graphene Paper from Perforated Graphene Oxide for Efficient Oxygen Reduction, *ACS Omega*, 2018, **3**(5), 5522–5530, DOI: 10.1021/acsomega.8b00400.

50 A. Dutta, R. Bera, A. Ghosh and A. Patra, Ultrafast Carrier Dynamics of Photo-Induced Cu-Doped CdSe Nanocrystals, *J. Phys. Chem. C*, 2018, **122**(29), 16992–17000, DOI: 10.1021/acs.jpcc.8b05422.

51 A. Ganguly, S. Sharma, P. Papakonstantinou and J. Hamilton, Probing the thermal deoxygenation of graphene oxide using high-resolution in situ X-ray-based spectroscopies, *J. Phys. Chem. C*, 2011, **115**(34), 17009–17019.

52 X. Liu, X. Jin, H. Deng, Z. Sha and X. Zhou, Formation of nitrogen-doped blue- and green-emitting fluorescent carbon dots via a one-step solid-phase pyrolysis, *J. Nanopart. Res.*, 2021, **23**, 45, DOI: 10.1007/s11051-021-05162-z.

53 U. K. Ghorui, G. Sivaguru, M. Sk, R. Thapa, M. A. Sampath and S. Chakrabortty, Defect-Engineered N-Doped Graphene Oxide-ZnWO4 Nanocuboids: Advancing Oxygen Reduction and Photo-Assisted Methanol Oxidation Reactions, *Small*, 2025, **21**, 2505511, DOI: 10.1002/smll.202505511.

54 H. Yang, H. Wang, L. Wang, M. Sun, F. Xu, H. Ye, J. Ren and Z. Y. Yuan, Optimized electronic structure induced by cobalt metaphosphate/phosphide for highly efficient hydrazine-assisted water splitting at high current densities, *J. Colloid Interface Sci.*, 2025, **695**, 137765, DOI: 10.1016/j.jcis.2025.137765.

55 M. Chen, M. Y. Zhao, F. M. Liu, R. Wan, X. Qian, X. Zhang, Z. Y. Yuan, C. S. Li and X. Y. Li, Mesoporous Ni3S2@Ni-incorporated and N-doped carbon nanohorn-carbon nanosheets: heterostructure construction and electron modulation for an efficient electrocatalyst for the oxygen evolution reaction, *Phys. Chem. Chem. Phys.*, 2025, **27**, 21329–21335.

56 G. Sivaguru, U. K. Ghorui, A. Mangalasseri, S. Reza, R. Dutta, S. Ghosh, G. K. Dalapati, R. Thapa and S. Chakrabortty, Cation Substituted Entropy Driven Cu–Mn–Zn–Cr–O Metal Oxide for Efficient Seawater Splitting and Hybrid Supercapacitors, *Small*, 2025, 10306, DOI: 10.1002/smll.202510306.

57 W. Zheng, iR Compensation for Electrocatalysis Studies: Considerations and Recommendations, *ACS Energy Lett.*, 2023, **8**(4), 1952–1958, DOI: 10.1021/acsenergylett.3c00366.

58 S. Anantharaj and S. Noda, iR drop correction in electrocatalysis: everything one needs to know!, *J. Mater. Chem. A*, 2022, **10**, 9348–9354, DOI: 10.1029/D2TA01393B.

59 J. Yang, C. Wang, H. Ju, Y. Sun, S. Xing, J. Zhu and Q. Yang, Integrated Quasiplane Heteronanostructures of MoSe2/Bi2Se3 Hexagonal Nanosheets: Synergetic Electrocatalytic Water Splitting and Enhanced Supercapacitor Performance, *Adv. Funct. Mater.*, 2017, **27**, 1703864, DOI: 10.1002/adfm.201703864.

60 B. B. Kamble, A. De, S. J. Jang, A. Karmkar, V. Vinothkumar, N. Mujawar, S. Kundu and T. H. Kim, Structural Design of MOF-Based and MOF-Derived Composites for Oxygen Evolution Electrocatalysis: Materials Innovation for Energy and Environmental Sustainability, *Energy Environ. Mater.*, 2026, 70264, DOI: 10.1002/eem2.70264.

61 B. Mohanty, A. Mitra, B. Jena and B. K. Jena, MoS2Quantum Dots as Efficient Electrocatalyst for Hydrogen Evolution Reaction over a Wide pH Range, *Energy Fuels*, 2020, **34**(8), 10268–10275, DOI: 10.1021/acs.energyfuels.0c01283.

62 S. Kumari, N. Sunaina, S. Devi and M. Jha, Design of New Process for Anchoring Carbon Quantum Dots onto the Cobalt Oxyhydroxide Surface for Efficient Oxygen Generation, *Energy Fuels*, 2025, **39**(13), 6426–6437, DOI: 10.1021/acs.energyfuels.4c05203.

63 A. Lasia, The Origin of the Constant Phase Element, *J. Phys. Chem. Lett.*, 2022, **13**(2), 580–589, DOI: 10.1021/acs.jpclett.1c03782.

64 S. S. Jeon, P. W. Kang, M. Klingenhof, H. Lee, F. Dionigi and P. Strasser, Active Surface Area and Intrinsic Catalytic Oxygen Evolution Reactivity of NiFe LDH at Reactive Electrode Potentials Using Capacitances, *ACS Catal.*, 2023, **13**(2), 1186–1196, DOI: 10.1021/acscatal.2c04452.

65 P. J. J. Sagayaraj, S. Kavinkumar, K. Oyama, N. Okibe, H. Il Kim and K. Sekar, Extending the accessibility of catalytic active sites through l-cysteine assisted sulfidation for promoting the hydrogen evolution reaction, *Energy Adv.*, 2024, **4**, 296–303, DOI: 10.1039/D4YA00578C.

66 U. K. Ghorui, B. Show, D. Roy, A. Basak, B. Adhikary and A. Mondal, Strategically Designed Pd-Induced Changes in Alkaline Hydrogen Evolution Reaction and Oxygen Evolution Reaction Performances of Electrochemical Water Oxidation by the Galvanically Synthesized MoO2/MoO3 Composite Thin Film, *ACS Appl. Mater. Interfaces*, 2024, **16**, 3460–3475.

67 Y. Gui, Z. Liu, X. Feng, Y. Jia, Y. Zhang, Y. Zhang, H. Yang, Y. Zhang, M. Li, L. Liang and J. W. Shi, One-step electrodeposition synthesis of NiFePS on carbon cloth as self-supported electrodes for electrochemical overall water splitting, *J. Colloid Interface Sci.*, 2024, **673**, 444–452, DOI: 10.1016/j.jcis.2024.06.096.

68 N. Selvaraju, K. Ravichandran and G. Venugopal, A short review of the kinetic parameters of carbon quantum dots for Electrocatalytic Hydrogen evolution reaction, *Int. J. Hydrogen Energy*, 2023, **48**, 3807–3823, DOI: 10.1016/j.ijhydene.2022.10.203.

69 Y. Lei, C. Yang, J. Hou, F. Wang, S. Min, X. Ma, Z. Jin, J. Xu, G. Lu and K. W. Huang, Strongly coupled CdS/graphene quantum dots nanohybrids for highly efficient photocatalytic hydrogen evolution: Unraveling the essential roles of graphene quantum dots, *Appl. Catal., B*, 2017, **216**, 59–69, DOI: 10.1016/j.apcatb.2017.05.063.

70 R. Bose, V. R. Jothi, K. Karuppasamy, A. Alfantazi and S. C. Yi, High performance multicomponent bifunctional catalysts for overall water splitting, *J. Mater. Chem. A*, 2020, **8**, 13795–13805.